IEEE Access
Multidisciplinary | Rapid Review | Open Access Journal

Received July 25, 2018, accepted September 12, 2018, date of publication September 17, 2018, date of current version October 12, 2018.

Digital Object Identifier 10.1109/ACCESS.2018.2870562

Real-Time Spectrum Sniffer for Cognitive Radio Based on Rotman Lens Spectrum Decomposer

XIAOYI WANG, (Student Member, IEEE), ALIREZA AKBARZADEH, LIANFENG ZOU, AND CHRISTOPHE CALOZ, (Fellow, IEEE)
Department of Electrical Engineering, Polytechnique Montréal, Montreal, QC H3T 1J4 , Canada
Corresponding author: Xiaoyi Wang (xiaoyi.wang@polymtl.ca)

ABSTRACT We introduce the concept of an energy-detection Rotman-lens spectrum decomposer (RLSD) real-time spectrum-sniffer (RTSS) for cognitive radio. Compared to a previously existing RTSS, the RLSD-RTSS offers the advantages of being 1) Based an a simpler and lower-cost purely passive structure, 2) Easier to design and easily amenable to tunability, 3) Of much broader bandwidth, and 4) Of accommodating more channels. The electrical size of the device is electrically larger, but perfectly acceptable in the millimeter-wave frequency range. The proposed RLSD-RTSS is demonstrated theoretically and experimentally, and is shown to support tunability in terms of both bandwidth-resolution and operation band. Given its unique features, this device may find wide applications in 5G UHD and 3-D video systems.

INDEX TERMS Spectrum sniffing, real-time spectrum-sniffer (RTSS), Rotman lens, Rotman-lens spectrum decomposer (RLSD), cognitive radio, 5G wireless systems.

I. INTRODUCTION

Future wireless communication systems will need drastic enhancements to accommodate anticipated end-user speed and reliability requirements. Reconfiguration strategies, globally referred to as *cognitive radio* [1], may become a pivotal approach to address this challenge in forthcoming 5G systems, especially in applications with extremely high throughput, such as UHD and 3D video [2].

Cognitive radio consists in two main operations: first sensing – or "*sniffing*" – the ambient spectrum so as to identify white (free) bands in it, and next reconfigure the radio system to exploit these white bands for optimal spectral efficiency at all times.

The spectrum sniffing operation has been traditionally performed in a digital manner, using energy detection, matched-filter detection, cyclostationary-feature detection or spatio-temporal spectrum occupation detection [3]–[6]. However, as the operating frequency gets higher and the operating bandwidth becomes wider, as is typically the case in the millimeter-wave regime, spectrum sniffing should be realized in an *ultra-fast* fashion. In such situations, digital approaches may be just too slow, or excessively expensive and power hungry, and an *alternative technology is hence required*.

Real-time analog processing (RAP), which consists in manipulating electromagnetic signals in real-time using agile microwave dispersive components called "phasers," appears to be a promising technology in this regard [7]. Phasers have been recently realized in different forms, including C-sections and D-sections [8]–[12], coupled resonators [13], [14], nonuniform delay lines [15], metamaterial transmission-line structures [16], loss-gain pairs [17], and RAP has been used in several applications, including compressive receiving [16], real-time spectrum analysis [18], [19], real-time spectrum sniffing [20], Hilbert transforming [21], SNR enhanced impulse radio transceiving [22], dispersion code multiple access (DCMA) [23], signal encryption [24], radio-frequency identification [25] and scanning-rate control in antenna arrays [26].

Recently, an energy-detection Real-Time Spectrum Sniffer (RTSS) based on a mixer and a coupled-line phaser with stair-case group delay response has been reported in [27]. However, this sniffer is limited by the following features: requirement for an auxiliary pulse generator and of a local oscillator source for mixing, high design complexity and lack of tunability, restricted bandwidth, and small number of channels.

In this paper, we present an alternative energy-detection RTSS, based on an Rotman Lens Spectrum Decomposer (RLSD) [19], [28]. This device resolves all the aforementioned issues of the RTSS in [27], and is hence very promising for future communication systems: 1) it is based on a simple passive structure, the RLSD, requiring neither

mixers nor sources, and it is hence inexpensive; 2) it is easy to design and may be tuned in real-time using PIN diodes and switches; 3) it exhibits a very broad bandwidth, due to its true-time delay nature; 4) it may accommodate a great number of channels.

The paper is organized as follows. Section II presents the principle of the proposed RTSS. Section III recalls the fundamental aspects of the RLSD that constitutes the key component of the RTSS. Section IV shows the resolution control capabilities of the RLSD-RTSS, which include resolution uniformity, bandwidth resolution trade-off tuning and operation band tuning. The RLSD-RTSS is demonstrated in Sec. V, and Sec. VI concludes the paper.

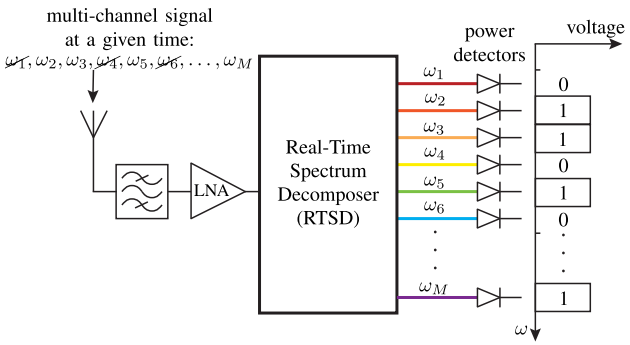

FIGURE 1. Principle of the proposed real-time spectrum sniffer (RTSS).

II. REAL-TIME SPECTRUM SNIFFER (RTSS) PRINCIPLE

The principle of the proposed real-time spectrum sniffer (RTSS) is presented in Fig. 1. The broadband-spectrum (multi-channel) ambient signal to sniff is picked up by an omnidirectional antenna, amplified and passed through a real-time spectrum decomposer (RTSD). The RTSD operates like a prism, i.e. separates out in space, towards different output ports, (and in real-time) the different frequencies composing the input signal are corresponding to different communication channels. The so-separated output signals are then detected by power detectors, from which the binary information on the activity (bit 1) or inactivity (bit 0) of all the channels is instantaneously provided in the base-band domain.

III. ROTMAN LENS SPECTRUM DECOMPOSER (RLSD)

The key component in the RTSS of Fig. 1 is the real-time spectrum decomposer (RTSD). We propose here to realize this RTSD in the form of the ray-optics structure shown in Fig. 2. This structure is composed by the interconnection of a Rotman lens [29]–[33] and a reflective dispersive transmission line array [34].

The basic operation of the lens RTSD is as follows. The ambient broadband input signal is injected into the system from a port at the left center of the lens and then cylindrically radiates within the lens to the ports at its right. The (full-spectrum) signals reaching these ports are then reflected by an array of transmission lines with different lengths. Due to the

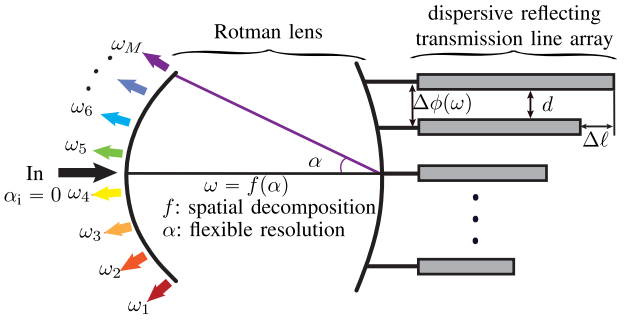

FIGURE 2. Implementation of the real-time spectrum decomposer (RTSD) in Fig. 1 based on a Rotman lens and a dispersive reflecting transmission line array (lens RTSD).

dispersive nature of this array reflector [34], a phase gradient is formed on the right ports, causing the wave to decompose towards the left, with different frequencies reaching different ports, so as to achieve the desired spectral decomposition.

Calling $\Delta\ell$ the length difference between adjacent transmission lines in Fig. 2, the phase gradient after round-trip reflection from the dispersive transmission line array is found as

$$\Delta\phi_{\text{array}}(\omega) = 2\beta_{\text{e}}(\omega)\Delta\ell = \frac{2\omega\sqrt{\epsilon_{\text{e}}}}{c}\Delta\ell, \tag{1}$$

where $\beta_{\text{e}}(\omega)$ is the effective wavenumber of the transmission lines. Assuming that $\Delta\ell$ is designed to be N times (N integer) half the wavelength at the frequency intended to scatter at the center of the RLSD left contour, ω_0, i.e.

$$\Delta\ell = N\lambda_0/2 = N\pi c/(\sqrt{\epsilon_{\text{e}}}\omega_0), \quad N = 1, 2, 3, \ldots, \tag{2}$$

we find, upon substitution into (1),

$$\Delta\phi_{\text{array}}(\omega) = 2\pi N\frac{\omega}{\omega_0}. \tag{3}$$

On the other hand, according to antenna array theory, the function $\Delta\phi_{\text{lens}}(\omega)$ for beam forming at the angle ψ is

$$\Delta\phi_{\text{lens}}(\omega) = \frac{\omega}{c}d\sin\psi = \frac{\omega}{c}d\gamma\sin\alpha, \tag{4}$$

where the latter equality stems from the Rotman lens beam former relationship [29]

$$\gamma \approx \frac{\sin\psi}{\sin\alpha}, \tag{5}$$

with α being the port position angle, as shown in Fig. 2.

$\Delta\phi_{\text{lens}}(\omega)$ represents the phase gradient at the right contour of the Rotman lens that is required for the frequency ω to radiate into the direction α, as required for spectral decomposition. This gradient must be compatible with the phase gradient after reflection from the dispersive array, $\Delta\phi_{\text{array}}$. For this to be the case, we equate (3) and (4), and consider the fact that the phase is periodic,

$$2\pi N\frac{\omega}{\omega_0} = \frac{\omega}{c}d\gamma\sin\alpha + 2\pi n \quad (n \text{ integer}), \tag{6}$$

which yields the following relation for the frequency (ω) versus port position (α) law of the lens RTSD:

$$\omega_n(\alpha) = \frac{2\pi n\omega_0 c}{2\pi Nc - \omega_0 d\gamma \sin\alpha}. \quad (7)$$

In practice, one would use $n = 1$ in this equation, since $n > 1$ corresponds to harmonics of ω_1, whose re-scaling to ω_1 for a center frequeny of ω_0 would imply larger physical size. In the following, we shall drop the subscript n, which is implicitly to assumed to be equal to 1.

IV. RTSD RESOLUTION CONTROL

A. UNIFORM RESOLUTION DESIGN

If the output ports of the lens RTSD are equidistant, i.e. $\Delta\alpha = \alpha_{k+1} - \alpha_k$ = constant in Fig. 2, the resolution across the spectrum of the input signal is nonuniform [28], which is most often not desired in practice. Therefore, we shall distribute the output ports in such a fashion that the RTSD exhibits *uniform resolution* [19].

For the sake of concreteness, let us develop the overall RTSD resolution control theory through a specific design example. Consider an RTSS operating around $f_0 = \omega_0/(2\pi) = 40$ GHz with bandwidth resolution of about 15 GHz, and $M = 8$ output ports (Fig. 1), with the parameters $N = 2$, $d = \lambda_0/2$ or $d = c/(2f_0)$ and $\gamma = 1$. Inserting these parameters in (7) leads to the frequency versus position relation plotted in Fig. 3.

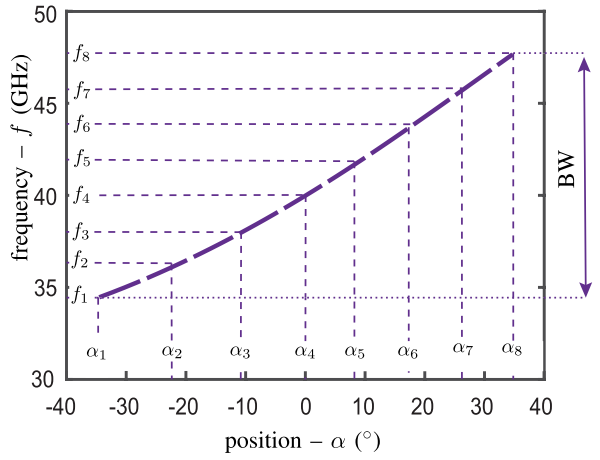

FIGURE 3. Frequency (f) versus port position (α) of the lens RTSD in Fig. 2, obtained by (7), with $f_0 = \omega_0/(2\pi) = 40$ GHz, $N = 2$ and $\gamma = 1$. The discrete port positions for *uniform-resolution* [$\Delta f_k = f_{k+1} - f_k = \Delta f$ = const. ($k = 1, \ldots, 7$)] are shown for $N = 2$.

Achieving resolution uniformity simply consists in uniformly sampling the curve $f(\alpha)$ in Fig. 3 along the vertical (frequency–f) axis and reading out the corresponding angular positions on the horizontal (position–α) axis. The values α_n obtained in this fashion directly provide the locations of the ports on the left contour of the lens RTSD producing uniform resolution.

The 8-channel uniform-resolution lens RTSD is then designed in microstrip technology on a Rogers 6002 substrate

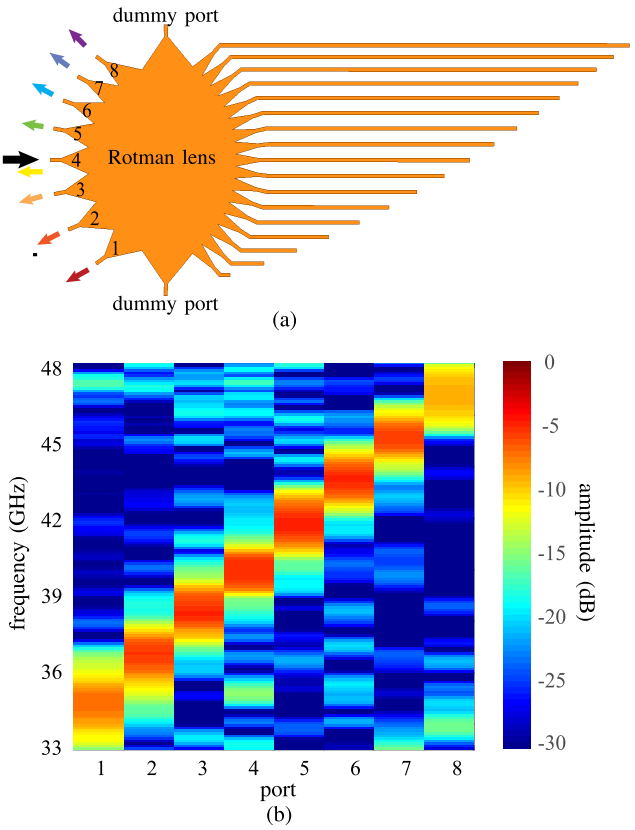

FIGURE 4. Uniform-resolution 8-channel RTSD lens. (a) Layout. (b) Full-wave simulated spectrum versus lens port.

with thickness 0.254 mm, dielectric constant 2.94 and loss tangent 0.0012. The resulting layout is shown in Fig. 4(a). The Rotman lens includes 8 input ports, 15 output ports and 2 dummy ports (reducing spurious reflection [29]). The 3 focal angles [29] are 0°, $\alpha_0 = 35°$ and $-\alpha_0 = -35°$, with focal length 28.4 mm, 25.6 mm and 25.6 mm, respectively, which are chosen as trade-offs between device size and number of ports of the Rotman lens. The 15 50-Ω transmission lines are directly connected to the output ports of the Rotman lens with uniform width of 0.66 mm and adjacent line length difference of 4.8 mm, obtained from (2).

Figure 4(b) plots the full-wave simulated spectrum versus port of the RTSD lens in Fig. 4(a). It shows that the lens RTSD essentially operates as expected, despite some spurious inter-port leakage due to small mismatch at the lens to strip transitions and resulting inter-port coupling. This effect may be mitigated by using longer or more efficient (e.g. exponential or Klopfenstein [35]) transitions.

B. BANDWIDTH-RESOLUTION TUNING

Tuning the length difference $\Delta\ell$ of the reflecting array transmission lines [Eq. (1)], or equivalently tuning N since $\Delta\ell \propto N$ [Eq. (2)], tunes the phase gradient $\Delta\phi_{\text{array}}$ of the array [Eq. (3)], which results in altering the receiving angle versus frequency sensitivity, $s(N) = \partial\alpha/\partial\omega$ and hence the bandwidth of the RTSS. Specifically, increasing N increases

the array dispersion and lens diffraction, i.e. splits frequencies more over space or increases $s(N)$, which decreases the RTSS bandwidth, BW= $[\omega(-\alpha_0), \omega(\alpha_0)]$, since the extremal frequencies of the test pulse are pushed beyond the receiving area ($[-\alpha_0, \alpha_0]$) of the lens. So, we should have BW $\propto 1/s \propto \partial\omega/\partial\alpha \propto 1/N$.

Let us verify this mathematically by deriving (7)

$$\mathrm{BW}(N) \propto \frac{\partial\omega}{\partial\alpha} = \frac{2\pi\omega^2 d\gamma\cos\alpha}{(2\pi Nc - \omega_0 d\gamma\sin\alpha)^2}. \tag{8}$$

This expression is rather complicated, but its evaluation about the center port of the RTSS, $\alpha = 0$, leads to the much simpler result

$$\mathrm{BW}(N) \propto \left.\frac{\partial\omega}{\partial\alpha}\right|_{\alpha=0} = \frac{\omega_0}{2N}, \tag{9}$$

which confirms the predicted trend of the bandwidth being inversely proportional to N.

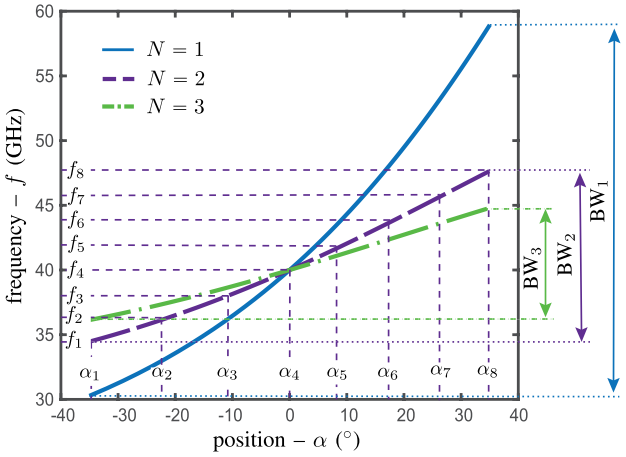

FIGURE 5. Frequency (f) versus port position (α) of the lens RTSD in Fig. 2, computed by (7) for $N = 1, 2, 3$ in (2) with $f_0 = \omega_0/(2\pi) = 40$ GHz. The bandwidths for $N = 1, 2, 3$ are [30.5, 58.5] GHz, [35.0, 46.7] GHz and [36.2, 43.5] GHz, respectively.

Figure 5 plots the function $\omega(\alpha)$ given by (7) for $N = 1, 2, 3$, where $N = 2$ corresponds to the design in Fig. 3. By design [from (3) $\Delta\phi_{\mathrm{array}}(\omega = \omega_0) = 2\pi N$, yielding the same radiation pattern, with main beam pointing to $\alpha = 0$, $\forall$ N] the three curves intersect at the point $(0, f_0) = (0°, 40\ \mathrm{GHz})$, and the operating frequency range indeed increases with decreasing N. The operation bandwidth for $N = 1$ is almost five times larger than that for $N = 3$, and this ratio would naturally increases with larger N. This represents a very large bandwidth tuning capability, where one can trade bandwidth for resolution and vice-versa.

Figure 6 plots the full-wave simulated spectra versus lens port number in the RTSD of Fig. 4(a) for $N = 1$ and $N = 3$, complementing the results for $N = 2$ in Fig. 4(b). One first observes that the operation bandwidths correspond to the theoretical predictions in Fig. 5. The second observation is that the amount of parasitic leakage increases with decreasing N.

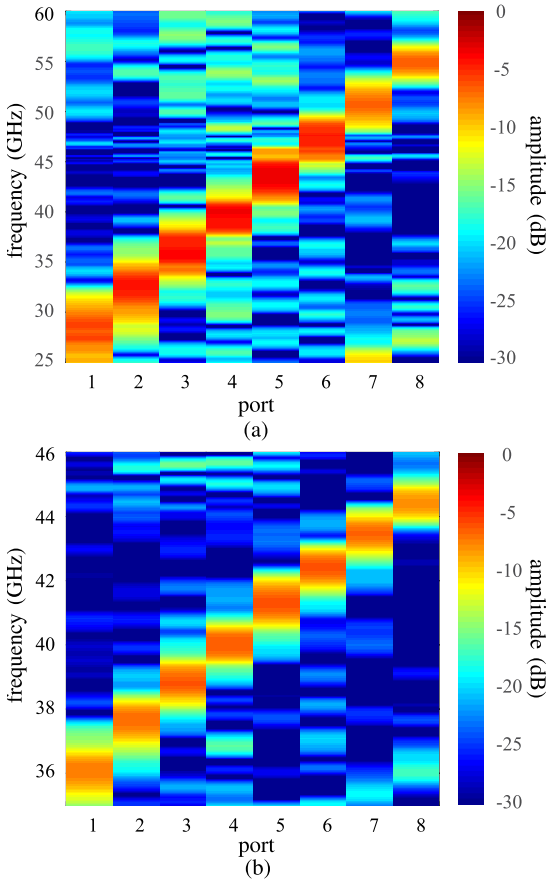

FIGURE 6. Full-wave simulated spectra versus lens port number in the RTSD of Fig. 4(a) for different values of N. (a) $N = 1$. (b) $N = 3$. The result for $N = 2$ is plotted in Fig. 4(b).

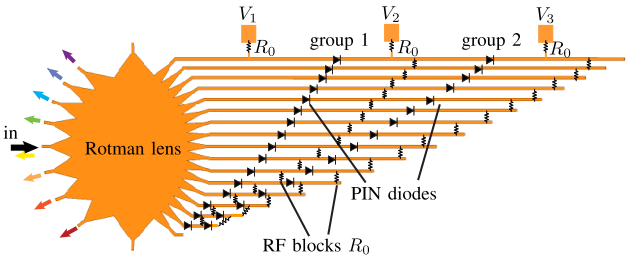

FIGURE 7. Implementation of a 3-mode ($N = 1, 2, 3$ in Fig. 5) bandwidth-resolution tuning by RLSD-RTSS using 2 PIN diodes in each reflecting line.

This is simply understood by remembering that the bandwidth is inversely proportional to N [Eq. (9)] and realizing the limited bandwidth of the transitions between the lens and the microstrip lines on both sides of the lens.

Practically, the bandwidth-resolution tuning demonstrated in this section can be straightforwardly implemented by multiplying all the lengths of the reflecting array transmission lines by N and connecting the resulting N sections by PIN diodes. For instance, in the case of a 3-mode tunability design, illustrated in Fig. 7, 3 different DC voltages, V_1, V_2 and V_3, are used to control the ON and OFF states of the PIN diodes via resistors R_0 with high resistance value so as to pass the

DC signals and block the RF signals. If $V_1 > V_2 + \phi_0 > V_3 + 2\phi_0$ (ϕ_0: built-in potential), all the diodes are ON, which leads to the longest lines, corresponding to the highest RTSS resolution according to Fig. 5 ($N = 3$). Let us call this mode mode A. If $V_1 > V_2 + \phi_0$ but $V_2 + \phi_0 < V_3$, then the diodes of group 1 are ON while diodes of group 2 are OFF, leading to a medium-resolution ($N = 2$) mode, mode B. Finally, of $V_1 < V_2 + \phi_0$, then the diodes in the group 1 are OFF, leading to the lowest resolution ($N = 1$) mode, mode C. Assuming that all the diodes are identical, their loss does not influence the location of the focal points [Eq. (7)]; it only (equally) increases the insertion loss at all the output ports, which will leads to lower output power in all output ports in Fig. 4(b) and Fig. 6, and may hence require higher-sensitivity detectors.

C. OPERATION BAND TUNING

Until this point, the input port has always been fixed to the middle of the left contour of the Rotman lens, i.e. $\alpha_i = 0$, as shown in Fig. 2. Switching the input position between the ports the RTSS, i.e. letting $\alpha_i = \alpha_k$ with k *varying* between $k = 1$ to $k = M$, slides the operating spectrum and hence allows sniffing different frequency bands. Indeed, such switching changes the optical path lengths across the structure, effectively adding an extra term to the array phase gradient $\Delta\phi_{\text{array}}$ in (3), which results in rotating the spectrum around the Rotman lens and hence the part of the spectrum falling into the port sector $[-\alpha_0, \alpha_0]$.

The phase gradient term added by switching the input position is, according to the Rotman lens theory [29], $\omega\gamma d \sin\alpha_i/c$. Equation (3) generalizes then to

$$\Delta\phi_{\text{array}}(\omega) = 2\pi N\frac{\omega}{\omega_0} - \frac{\omega}{c}\gamma d \sin\alpha_i, \tag{10}$$

which in turn generalizes Eq. (7) to

$$\omega(\alpha) = \frac{2\pi\omega_0 c}{2\pi Nc - \omega_0 d\gamma(\sin\alpha + \sin\alpha_i)}. \tag{11}$$

This relation confirms that increasing α_i from $-\pi/2$ to $\pi/2$ increases the frequency at any port, α_k.

Figure 8 plots the function $\omega(\alpha)$ given by (11) for different values of α_i. It confirms the predicted operation band tuning. Moreover, it shows the the bandwidth varies little with α_i.

Figure 9 plots the full-wave simulated spectra versus input port position in the RTSD of Fig. 4(a) for $\alpha_i = -35°$ and $\alpha_i = 35°$, complementing the results for $\alpha_i = 0°$ in Fig. 4(b). The operation bands and bandwidths correspond to the theoretical predictions in Fig. 8.

Practically, the operation band tuning demonstrated in this section may be implemented using a switching matrix and circulators, as shown in Fig. 10 and understood from Fig. 8. When the switching matrix is switched to port 1 ($\alpha_i > 0$, $|\alpha_i|$ maximum), the RTSS has the largest operating frequency. As the switching matrix is switched from port 1 to port 8, the RTSS operating frequency gradually decreases. When the switching matrix is switched to port 8 ($\alpha_i < 0$, $|\alpha_i|$ maximum), the RTSS has the smallest operating frequency.

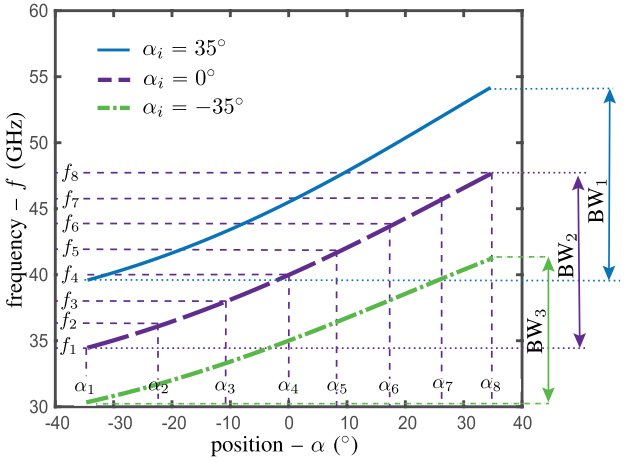

FIGURE 8. Frequency (f) versus port position (α) of the lens RTSD in Fig. 2, computed by (11) for $\alpha_i = -35°, 0, 35°$, with $f_0 = \omega_0/(2\pi) = 40$ GHz and $N = 2$.

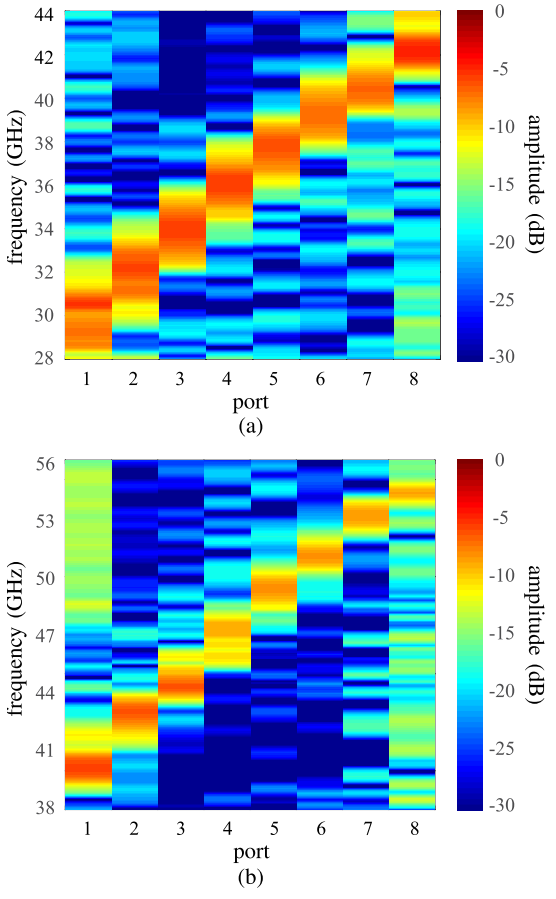

FIGURE 9. Full-wave simulated spectra versus lens port number in the RTSD of Fig. 4(a) for different values of α_i. (a) $\alpha_i = -35°$, or port 1 (bottom) in Fig. 4. (b) $\alpha_i = 35°$, or port 8 (top) in Fig. 4.

V. DEVICE DEMONSTRATION

The RLSD of Fig. 4 was fabricated and measured. Figure 11(a) shows the prototype while Fig. 11(b) plots the corresponding measured spectrum versus output port number. The measured spectrum distribution agrees very well with the theoretical prediction in Fig. 4(b) at least down to −15 dB.

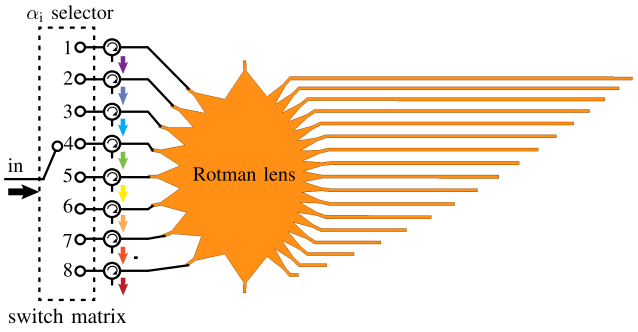

FIGURE 10. Implementation of operation band tuning RTSD-RTSS α_i using a switching matrix and circulators.

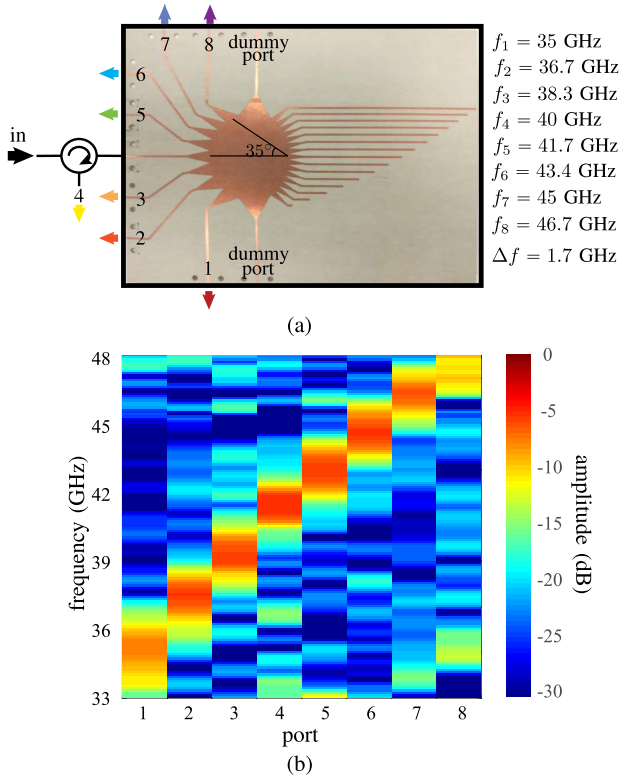

FIGURE 11. Spectral decomposition provided by the lens RTSD in Fig. 3 ($M = 8$) with $N = 2$ and uniform resolution. (a) Fabricated prototype. (b) Measured spectrum distribution versus lens port number.

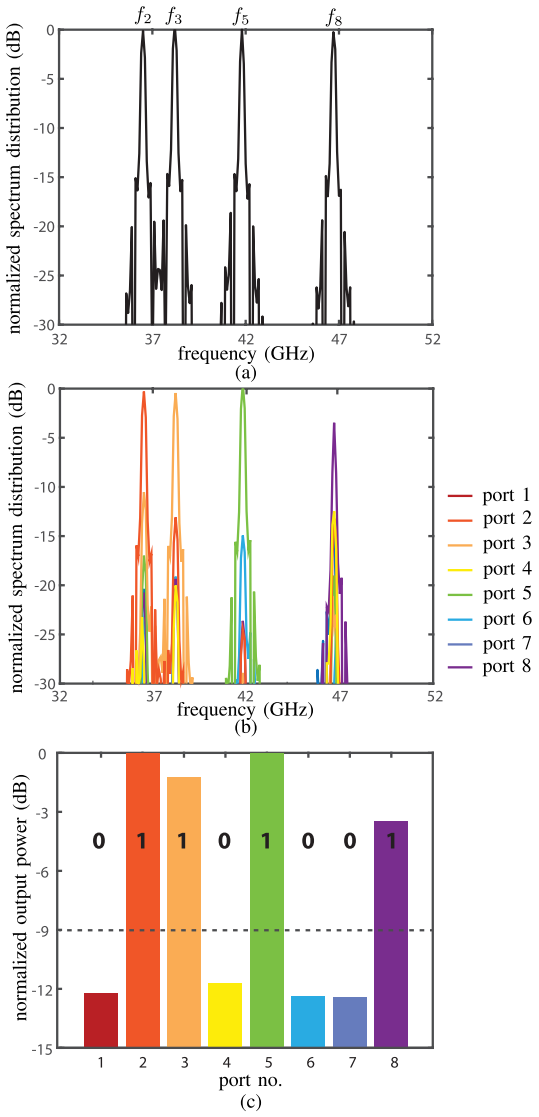

FIGURE 12. Experimental results for the RTSS (Fig. 1) with the lens RTSD prototype in Fig. 11. (a) Spectrum of the multi-channel input signal, with active channels $f_2 = 36.7$ GHz, $f_3 = 38.3$ GHz, $f_5 = 41.7$ GHz and $f_8 = 46.7$ GHz. (b) Spetrum of the output signals just before the detectors in Fig. 1. (c) Normalized energy of the output signals at all the ports, obtained by integrating the spectra corresponding to each of the ports in (b).

Figure 12(a) plots the spectra of the signals to detect[1] at the input of the RTSS (Fig. 1), corresponding to the 4 active channels $f_2 = 36.7, f_3 = 38.3, f_5 = 41.7$ and $f_8 = 46.7$ GHz. Figure 12(b) plots the spectra of the signals at all the output ports of the fabricated prototype (Fig. 11) just before the detectors (Fig. 1). It may be observed that each port exhibits an energy peak at the frequency of the corresponding channel if active, as expected, but also includes some energy from other active channels. This is a result of port-to-port leakage due to lens imperfection. For example port 2 (red color), essentially emanating from channel 2 (or f_2) [Fig 12(a)], has an energy peak around f_2, but it also includes some energy at f_2, f_5 and f_8, which correspond to leakage from the active channels 2, 5 and 8. This leakage effect translates into "detection noise" in the overall RTSS. Finally, Fig. 12(c) plots the energy detected at all the ports, with successful channel detection ensured with a threshold ideally placed near -9 dB below the level of the strongest signal.[2] Note that, since the input signals are here assumed to be equal,[3]

[1] In a real spectrum sniffing scenario, these signals are all mixed together and are hence indistinguishable from each other.

[2] The difference in the strengths of the different active-channel signals is exclusively due to imperfections of the RTSS prototype, since the input levels are identical [Fig. 12(a)].

[3] If this was not the case, then the positioning of the threshold would be more critical, requiring some optimization based on the knowledge of the environment.

our threshold depends only on the device and on its effective noise due to port-to-port leakage.

The implementation of the bandwidth-resolution tuning and operation band tuning versions of the RTSS demonstrated in Figs. 11 and 12 may be realized in the electronic architectures depicted in Fig. 7 and 10 has therefore not been implemented in the lab. Since these implementation would represent straightforward fabrication without added essential information, we have not implemented them. However, we have verified that the corresponding spectra of the fabricated prototype for all the tuning conditions in the operation band tuning RTSS and by full-wave simulation for the bandwidth-resolution tuning RTSS, and found, without surprise, excellent agreement in all cases.

VI. CONCLUSION

We have presented and demonstrated an energy-detection Rotman-lens spectrum decomposer (RLSD) real-time spectrum-sniffer (RTSS) for cognitive radio. This system has superior features compared to previous RTSS devices. Moreover, it is easily amenable to bandwidth-resolution tuning and operation band tuning. the RLSD RTSS may thus find wide applications in future communication systems, particularly in the millimeter-wave frequency range where the device size is perfectly accommodatable.

REFERENCES

[1] Y.-C. Liang, K.-C. Chen, G. Y. Li, and P. Mahonen, "Cognitive radio networking and communications: An overview," *IEEE Trans. Veh. Technol.*, vol. 60, no. 7, pp. 3386–3407, Sep. 2011.

[2] A. Osseiran, J. F. Monserrat, and P. Marsch, *5G Mobile and Wireless Communications Technology*. Cambridge, U.K.: Cambridge Univ. Press, 2016.

[3] A. Ghasemi and E. S. Sousa, "Spectrum sensing in cognitive radio networks: Requirements, challenges and design trade-offs," *IEEE Commun. Mag.*, vol. 46, no. 4, pp. 32–39, Apr. 2008.

[4] D. Bhargavi and C. R. Murthy, "Performance comparison of energy, matched-filter and cyclostationarity-based spectrum sensing," in *Proc. IEEE 17th Int. Workshop SPAWC*, Jun. 2010, pp. 1–5.

[5] T. Yucek and H. Arslan, "A survey of spectrum sensing algorithms for cognitive radio applications," *IEEE Commun. Surveys Tuts.*, vol. 11, no. 1, pp. 116–130, 1st Quart., 2009.

[6] G. Ding, J. Wang, Q. Wu, S. Fei, and Y. Chen, "Spectrum sensing in opportunity-heterogeneous cognitive sensor networks: How to cooperate?" *IEEE Sensors J.*, vol. 13, no. 11, pp. 4247–4255, Nov. 2013.

[7] C. Caloz, S. Gupta, Q. Zhang, and B. Nikfal, "Analog signal processing: A possible alternative or complement to dominantly digital radio schemes," *IEEE Microw. Mag.*, vol. 14, no. 6, pp. 87–103, Sep. 2013.

[8] S. Gupta, A. Parsa, E. Perret, R. V. Snyder, R. J. Wenzel, and C. Caloz, "Group-delay engineered noncommensurate transmission line all-pass network for analog signal processing," *IEEE Trans. Microw. Theory Techn.*, vol. 58, no. 9, pp. 2392–2407, Sep. 2010.

[9] Q. Zhang, S. Gupta, and C. Caloz, "Synthesis of broadband dispersive delay structures formed by commensurate C- and D-sections," *Int. J. RF Microw. Comput.-Aided Eng.*, vol. 24, no. 3, pp. 322–331, May 2014.

[10] S. Gupta, Q. Zhang, L. Zou, L. J. Jiang, and C. Caloz, "Generalized coupled-line all-pass phasers," *IEEE Trans. Microw. Theory Techn.*, vol. 63, no. 3, pp. 1007–1018, Mar. 2015.

[11] Y. Horii, S. Gupta, B. Nikfal, and C. Caloz, "Multilayer broadside-coupled dispersive delay structures for analog signal processing," *IEEE Microw. Wireless Compon. Lett.*, vol. 22, no. 1, pp. 1–3, Jan. 2012.

[12] X. Wang, L. Zou, and C. Caloz, "Tunable C-section phaser for dynamic analog signal processing," in *Proc. 32nd URSI GASS*, Aug. 2017, pp. 1–3.

[13] Q. Zhang, S. Gupta, and C. Caloz, "Synthesis of narrowband reflection-type phasers with arbitrary prescribed group delay," *IEEE Trans. Microw. Theory Techn.*, vol. 60, no. 8, pp. 2394–2402, Aug. 2012.

[14] Q. Zhang, D. L. Sounas, and C. Caloz, "Synthesis of cross-coupled reduced-order dispersive delay structures (DDSs) with arbitrary group delay and controlled magnitude," *IEEE Trans. Microw. Theory Techn.*, vol. 61, no. 3, pp. 1043–1052, Mar. 2013.

[15] M. A. G. Laso *et al.*, "Real-time spectrum analysis in microstrip technology," *IEEE Trans. Microw. Theory Techn.*, vol. 51, no. 3, pp. 705–717, Mar. 2003.

[16] S. Abielmona, S. Gupta, and C. Caloz, "Compressive receiver using a CRLH-based dispersive delay line for analog signal processing," *IEEE Trans. Microw. Theory Techn.*, vol. 57, no. 11, pp. 2617–2626, Nov. 2009.

[17] L. Zou, S. Gupta, and C. Caloz, "Loss-gain equalized reconfigurable C-section analog signal processor," *IEEE Trans. Microw. Theory Techn.*, vol. 65, no. 2, pp. 555–564, Feb. 2017.

[18] S. Gupta, S. Abielmona, and C. Caloz, "Microwave analog real-time spectrum analyzer (RTSA) based on the spectral–spatial decomposition property of leaky-wave structures," *IEEE Trans. Microw. Theory Techn.*, vol. 57, no. 12, pp. 2989–2999, Dec. 2009.

[19] X. Wang, A. Akbarzadeh, L. Zou, and C. Caloz, "Flexible-resolution, arbitrary-input, and tunable Rotman lens spectrum decomposer," *IEEE Trans. Antennas Propag.*, vol. 66, no. 8, pp. 3936–3947, Aug. 2018.

[20] B. Nikfal, S. Gupta, and C. Caloz, "Increased group-delay slope loop system for enhanced-resolution analog signal processing," *IEEE Trans. Microw. Theory Techn.*, vol. 59, no. 6, pp. 1622–1628, Jun. 2011.

[21] X. Wang, L. Zou, Z.-L. Deck-Léger, J. Azaña, and C. Caloz, "Coupled loop resonator Hilbert transformer," in *Proc. IEEE Int. Symp. Antennas Propag.*, Jul. 2018, pp. 1–2.

[22] B. Nikfal, Q. Zhang, and C. Caloz, "Enhanced-SNR impulse radio transceiver based on phasers," *IEEE Microw. Wireless Compon. Lett.*, vol. 24, no. 11, pp. 778–780, Nov. 2014.

[23] L. Zou, S. Gupta, and C. Caloz, "Real-time dispersion code multiple access for high-speed wireless communications," *IEEE Trans. Wireless Commun.*, vol. 17, no. 1, pp. 266–281, Jan. 2018.

[24] X. Wang and C. Caloz, "Phaser-based polarization-dispersive antenna and application to encrypted communication," in *Proc. IEEE Int. Symp. Antennas Propag.*, Jul. 2017, pp. 2187–2188.

[25] S. Gupta, B. Nikfal, and C. Caloz, "Chipless RFID system based on group delay engineered dispersive delay structures," *IEEE Antennas Wireless Propag. Lett.*, vol. 10, pp. 1366–1368, Oct. 2011.

[26] G. Zhang, Q. Zhang, Y. Chen, T. Guo, C. Caloz, and R. D. Murch, "Dispersive feeding network for arbitrary frequency beam scanning in array antennas," *IEEE Trans. Antennas Propag.*, vol. 65, no. 6, pp. 3033–3040, Jun. 2017.

[27] B. Nikfal, D. Badiere, M. Repeta, B. Deforge, S. Gupta, and C. Caloz, "Distortion-less real-time spectrum sniffing based on a stepped group-delay phaser," *IEEE Microw. Wireless Compon. Lett.*, vol. 22, no. 11, pp. 601–603, Nov. 2012.

[28] Y. Zhang and V. Fusco, "Rotman lens used as a demultiplexer/multiplexer," in *Proc. 42nd Eur. Microw. Conf.*, Oct./Nov. 2012, pp. 164–167.

[29] W. Rotman and R. F. Turner, "Wide-angle microwave lens for line source applications," *IEEE Trans. Antennas Propag.*, vol. AP-11, no. 6, pp. 623–632, Nov. 1963.

[30] R. C. Hansen, "Design trades for Rotman lenses," *IEEE Trans. Antennas Propag.*, vol. 39, no. 4, pp. 464–472, Apr. 1991.

[31] R. Rotman, M. Tur, and L. Yaron, "True time delay in phased arrays," *Proc. IEEE*, vol. 104, no. 3, pp. 504–518, Mar. 2016.

[32] S. Vashist, M. K. Soni, and P. K. Singhal, "A review on the development of Rotman lens antenna," *Chin. J. Eng.*, vol. 2014, Jul. 2014, Art. no. 385385.

[33] J. Dong, "Microwave lens designs: Optimization, fast simulation algorithms, and 360-degree scanning techniques," Ph.D. dissertation, Virginia Tech, Blacksburg, VA, USA, 2009.

[34] M. K. Smit and C. V. Dam, "PHASAR-based WDM-devices: Principles, design and applications," *IEEE J. Sel. Topics Quantum Electron.*, vol. 2, no. 2, pp. 236–250, Jun. 1996.

[35] D. M. Pozar, *Microwave Engineering*, 4th ed. Hoboken, NJ, USA: Wiley, 2011.

XIAOYI WANG (S'17) was born in Xuzhou, Jiangsu, China, in 1989. He received the B.S. degree in electrical engineering from the University of Electronic Science and Technology of China in 2011 and the M.S. degree in electrical engineering from Fudan University in 2014. He is currently pursuing the Ph.D. degree with the Polytechnique Montréal. His current research focuses on real-time analog signal processing for future radio systems.

ALIREZA AKBARZADEH was born in Shiraz, Iran, in 1984. He received the B.Sc. degree from the Department of Electrical Engineering, Shiraz University, in 2006. In 2007, he moved to Singapore to pursue his postgraduate studies and received the M.Eng. degree from Nanyang Technological University in 2009 and the Ph.D. degree from the National University of Singapore (NUS) in 2014. During his Ph.D. studies, he spent three months in Scotland to collaborate with Prof. U. Leonhardt's research group at the University of St. Andrews. After graduating from NUS, he got an offer from Prof. C. Soukoulis to join the Photonic-, Phoninc-, Metamaterials Group, Foundation for Research and Technology-Hellas, Crete, Greece, where he held a Post-Doctoral Researcher from 2014 to 2017. During his first postdoctoral job, he had the opportunity to visit Iowa State University, USA, as a Visiting Scholar. Subsequent to his position in Greece, he got an offer from Prof. C. Caloz to join his group at the Polytechnique Montréal, Montreal, where he has been a Post-Doctoral Researcher.

LIANFENG ZOU received the B.Eng. degree in electromagnetic field and microwave technology from the University of Electronic Science and Technology of China, Chengdu, China, in 2004, the M.E. degree in electronic science and technology from the Graduate University of Chinese Academy of Sciences, Beijing, China, in 2007, and the Ph.D. degree from the Polytechnique Montréal, Montreal, QC, Canada, in 2017.

From 2007 to 2012, he was as an RF Engineer with the China Electronics Group Corporation. His research interests include dispersion engineered structures and their applications in the real-time analog signal processing for future millimeter-wave and terahertz radio systems.

CHRISTOPHE CALOZ (F'10) received the Diplôme d'Ingénieur en Électricité and the Ph.D. degree from the École Polytechnique Fédérale de Lausanne, Switzerland, in 1995 and 2000, respectively. From 2001 to 2004, he was a Post-Doctoral Research Fellow with the Microwave Electronics Laboratory, University of California at Los Angeles. In 2004, he joined the Polytechnique Montréal, where he is currently a Full Professor, the Holder of a Canada Research Chair (CRC) Tier-I, and the Head of the Electromagnetics Research Group.

In 2009, he co-founded the company ScisWave (now Tembo Networks). He has authored and co-authored over 700 technical conference, letter and journal papers, 17 books and book chapters, and he holds a dozen of patents. His works have generated about 20 000 citations, and he has been a Thomson Reuters Highly Cited Researcher. He was a member of the Microwave Theory and Techniques Society (MTT-S) Technical Committees MTT-15 (Microwave Field Theory) and MTT-25 (RF Nanotechnology), a Speaker of the MTT-15 Speaker Bureau, the Chair of the Commission D (Electronics and Photonics) of the Canadian Union de Radio Science Internationale and an MTT-S representative at the IEEE Nanotechnology Council. He has been a fellow of the Canadian Academy of Engineering since 2016. He received several awards, including the UCLA Chancellor's Award for Post-doctoral Research in 2004, the MTT-S Outstanding Young Engineer Award in 2007, the E.W.R. Steacie Memorial Fellowship in 2013, the Prix Urgel-Archambault in 2013, the Killam Fellowship in 2016, and many best paper awards with his students at international conferences. He has been the IEEE Distinguished Lecturer for the Antennas and Propagation Society (AP-S) since 2014. He was an Associate Editor of the TRANSACTIONS ON ANTENNAS AND PROPAGATION of AP-S from 2015 to 2017. In 2014, he was elected as a member of the Administrative Committee of AP-S. He was a Distinguished Adjunct Professor at King Abdulaziz University, Saudi Arabia, from 2014 to 2015.

His research interests include all fields of theoretical, computational and technological electromagnetics, with strong emphasis on emergent and multidisciplinary topics, such as particularly metamaterials and metasurfaces, nanoelectromagnetics, space-time electrodynamics, thermal radiation management, exotic antenna systems, and real-time radio/photonic processing.